Scilight

Advanced Characterization

https://www.sciltp.com/journals/ac

Article

Deciphering the "Thermal Snap" on Ultra-High Ni Cathodes via Multi-Modal *Operando* Synchrotron X-ray and Mass Spectrometry

Yuying Zhang [1,†], Hanwei Liu [1,†], Zhenzhong Li [1], Chao Wang [1], Wencheng Su [1], Wei Zhou [1], Jingfu He [1,*] and Chunzhen Yang [1,2,*]

[1] School of Materials, Sun Yat-sen University, Shenzhen 518107, China
[2] Laboratory of Synchrotron Radiation Techniques for Industrial Applications, Shenzhen 518107, China
* Correspondence: hejf27@mail.sysu.edu.cn (J.H.); yangchzh6@mail.sysu.edu.cn (C.Y.)
† These authors contributed equally to this work.

How To Cite: Zhang, Y.; Liu, H.; Li, Z.; et al. Deciphering the "Thermal Snap" on Ultra-High Ni Cathodes via Multi-Modal Operando Synchrotron X-ray and Mass Spectrometry. *Advanced Characterization* **2026**, *1*(1), 59–70.

Received: 24 April 2026
Revised: 30 May 2026
Accepted: 2 June 2026
Published: 10 June 2026

Abstract: Deciphering the fundamental triggers of thermal instability in ultra-high nickel cathodes is vital for advancing safe, high-energy-density lithium-ion batteries. In this work, we present a reaction device that enables operando synchrotron XRD, XAFS, and online mass spectrometry (OMS) measurements simultaneously, individually, or in paired combinations under identical heating and gas conditions. Using delithiated NCM96 as a model cathode, the complementary measurements correlate structural degradation, transition-metal redox evolution, and gas release during thermal decomposition, providing comprehensive insights into the thermal instability of high-nickel cathodes. Our findings reveal that thermal failure is a synergistic process initiated by electronic instability and the onset of lattice oxygen loss at approximately 175 °C. *Operando* XRD identifies a distinct H3-to-H2 structural relaxation and subsequent amorphization, while XAFS captures rapid Ni reduction and local coordination expansion between 185–330 °C. These electronic and local fluctuations drive the bulk phase transition from layered to spinel, which is tightly coupled with a dominant oxygen evolution event (O_{T1} comprising 74.9% of total O_2 release) and a vigorous exothermic response at ~210 °C. This study provides a refined mechanistic view of thermal instability of ultra-high Ni cathodes, offering a blueprint for the design of thermally safe high-nickel cathodes.

Keywords: *operando* XRD; online mass spectroscopy; thermal runaway; cathode materials; Ni-Co-Mn layered oxide

1. Introduction

Lithium-ion batteries (LIBs) have become the fundamental technology supporting the growth of electric vehicles (EVs) and large-scale energy storage systems [1]. As energy and power densities continue to improve, the thermal safety of batteries under complex conditions (e.g., overcharging, mechanical abuse, internal short circuits, and high temperatures) has become a critical issue [2–5]. Recent thermal runaway incidents in energy storage plants and EV batteries highlight that battery safety is now an engineering challenge affecting the stability of energy systems, thus becoming a bottleneck for the high-quality development of the new energy industry [6]. In practical applications, the pursuit of higher specific energy, faster charging capability, and wider operating windows has continuously narrowed the safety margin of LIBs [7,8]. Under these increasingly demanding conditions, local heat accumulation and parasitic reactions can be intensified, making it more difficult to suppress the initiation and propagation of thermal runaway [9]. Therefore, understanding the origin and evolution of thermal instability is essential for the safe deployment of next-generation LIB technologies.

Thermal runaway in LIBs is generally regarded as a self-amplifying process involving three stages: initial trigger (SEI decomposition at the anode), accelerated propagation (separator failure and internal short circuit), and final uncontrolled failure (cathode decomposition and intense heat release) [10–13]. Among these processes, the thermal decomposition of cathode materials under highly delithiated and elevated-temperature conditions is widely recognized as a critical step, because it is closely associated with intense heat generation and oxygen release [14]. This issue is particularly severe in high-nickel layered oxide cathodes, such as $LiNi_xCo_yMn_{1-x-y}O_2$ ($x > 0.6$, high-nickel NCM), which offer high capacity and low cost but suffer from deteriorated thermal stability at deep delithiation states. Previous studies have shown that charged high-nickel NCM can undergo layered structure degradation and subsequent transformation into spinel- and rock-salt-like phases, accompanied by oxygen release and transition-metal reduction [15–17]. More importantly, these processes are strongly coupled with changes in the local coordination environment and lattice stability. Once the cathode reaches a highly delithiated state, the weakened TM–O framework, enhanced cation migration tendency, and increased lattice oxygen activity can collectively facilitate structural collapse and oxygen evolution [18,19]. Therefore, cathode decomposition is not simply a consequence of thermal runaway, but a central process governing its escalation.

Despite various proposed mitigation strategies, including material doping, coating, and advanced thermal management, fully preventing accidents remains difficult due to a lack of clear understanding of the intrinsic reaction pathways and their dynamic coupling mechanisms [20–22]. To achieve inherent battery safety, it is vital to systematically uncover the correlations between structural evolution, electronic state changes, and oxygen release behaviors during thermal decomposition. Considerable efforts have been devoted to this issue from different experimental perspectives. Synchrotron-based time-resolved X-ray diffraction (XRD) studies have shown that charged high-Ni layered cathodes undergo progressive transformation of the layered framework into spinel- and rock-salt-like phases upon heating [23,24]. Further structural investigations suggested that this process may involve intermediate phases, such as the O1 phase or spinel-like domains, highlighting the structural complexity of thermally induced phase transitions in high-Ni cathodes [25]. In parallel, X-ray absorption fine structure spectroscopy (XAFS)-based studies have provided important insight into the local chemical-state evolution during thermal decomposition. These studies revealed that transition-metal reduction, particularly Ni reduction, occurs concurrently with structural degradation, indicating that electronic-state evolution is closely coupled to lattice instability [26]. They further showed that changes in local coordination environment and bond distances accompany the reduction process, demonstrating that short-range structural reorganization plays an important role in the thermal response of highly delithiated cathodes [27]. Gas-analysis and calorimetric studies have offered another important perspective. Using online mass spectrometry (OMS) or differential scanning calorimetry (DSC), previous work has identified pronounced oxygen release and exothermic behavior during the decomposition of charged high-Ni cathodes, and suggested that oxygen evolution is a key event governing the escalation of thermal runaway [28]. Additional studies further indicated that oxygen release may proceed in multiple stages and can be accompanied by the evolution of CO_2 and other gaseous species, implying that cathode decomposition involves not only lattice oxygen instability but also secondary interfacial or surface-related reactions [29–31].

However, most previous studies have focused on only one aspect of the decomposition process, such as long-range phase transition, transition-metal valence evolution, or gas release behavior. As thermal runaway is inherently a multiscale and multi-physics process, observations from a single technique are often insufficient to capture the full sequence of coupled reactions. For example, diffraction methods can reveal phase transitions and lattice collapse, but they are less sensitive to transient electronic-state evolution; XAFS can probe local coordination and valence changes, but cannot directly quantify gas evolution; gas analysis can track oxygen release, yet it does not directly identify the accompanying structural origin. Consequently, there remains a critical gap in correlating structural transformation, local chemical-state evolution, and gaseous product generation within the same thermal event.

To address these challenges, we developed an advanced *operando* synchrotron X-ray reaction apparatus for monitoring electrode behavior during thermal runaway. The apparatus is compatible with high-temperature XRD, XAFS, and OMS, enabling comprehensive characterization of structural, electronic, and gas-evolution processes in both cathode and anode materials. To verify its feasibility, operando XRD, XAFS, and OMS measurements were conducted separately on different XRD and XAFS beamlines using the same device under identical heating program and gas environment, allowing direct correlation of the complementary results. An NCM layered oxide with ultra-high Ni content ($LiNi_{0.96}Co_{0.02}Mn_{0.02}O_2$, Ni ~ 96%) was employed as the model cathode materials for thermal instability study. Ultimately, this approach offers a powerful tool to decode the fundamental mechanisms of cathode thermal decomposition and provides a scientific foundation for designing next-generation energy storage materials with enhanced safety.

2. Apparatus Design

As shown in Figure 1a, the custom-designed heating platform provides a consistent sample environment for all measurements. With optimized beamline configuration and equipment integration, the three techniques could ideally be performed simultaneously, enabling direct correlation of bulk phase transitions, local transition-metal electronic and coordination changes, and gas-evolution behavior as a function of temperature. To achieve these capabilities, the reaction cell was engineered to simultaneously satisfy several critical constraints, including optimized X-ray penetration, precision high-temperature control, efficient atmosphere regulation, and modular compatibility with various synchrotron beamlines. The internal architecture of the *operando* cell and its measurement configuration are detailed in Figure 1b,c, respectively.

(1) Reaction chamber design. To withstand high-temperature heating conditions, the reaction chamber is equipped with a small crucible made of Al_2O_3 or other high-temperature-resistant materials. This crucible features a 3 mm diameter hole at the bottom, enabling X-ray penetration for effective probing of the sample during heating. The back scattering window of the reaction chamber is designed with a 5–10 cm opening, allowing detection over a wider angular range for more precise measurements of X-ray diffraction or scattering signals. This setup ensures optimal conditions for in situ analysis of the material's behavior under thermal treatment. The detailed structure of the reaction chamber, including the front cover, cell body, gas inlet/outlet, heating module, temperature sensor, and water-cooling interfaces, is shown in Figure 1b.

(2) High-temperature heating and control. The heating unit is designed to ensure safe and stable operation during extended high-temperature testing. Heating wires and temperature probes are incorporated around the crucible to enable precise temperature ramping and real-time monitoring. A porous insulation layer further enhances temperature stability and reduces heat loss. To ensure the chamber's stability during experiments, it is sealed with high-temperature-resistant, X-ray-transparent materials. The system is capable of controlling a wide temperature range, enabling stable and uniform heating throughout the sample.

(3) Gas Environment and OMS Detection. To minimize dead volume and maximize detection efficiency by mass spectroscopy, the internal volume of the chamber is minimized. The system is connected to an OMS for real-time detection of trace gases, with an exhaust port for gas sampling. This compact design ensures quick response times and improved time resolution during the experiment. The system can utilize various carrier gases, such as Ar, O_2, or H_2, to create the desired atmosphere for *operando* testing. When argon is introduced, it quickly displaces the air in the chamber, achieving an argon concentration of over 99.9% within 10 min, providing a stable inert atmosphere for testing. The transient mass spectrometer used in the system tracks the release of gases, such as O_2, CO_2, CH_4, C_2H_5, and etc., allowing detailed tracking of gas evolution during thermal cycling.

(4) High-precision multi-axis displacement stage. The entire apparatus is mounted on a high-precision, multi-axis (xyz) displacement stage, which allows for precise alignment of the sample and rapid switching between different beamline platforms. This functionality enhances the versatility of the apparatus, making it adaptable to various synchrotron beamlines, enabling experiments at multiple beamlines without the need for extensive reconfiguration. As shown in Figure 1c, the assembled *operando* cell is mounted in a geometry that facilitates precise beam alignment and efficient collection of diffraction signals, which is essential for experiments across different synchrotron beamlines.

(5) Water cooling system. To maintain the integrity of the device and protect its sensitive components, the external metal chamber is equipped with a water-cooling system. This cooling system is controlled by a circulating chiller unit, maintaining the temperature at around 15 °C, and preventing overheating of the external structure, which contains electrical and gas lines. The water-cooling system effectively reduces thermal stress, prolonging the lifespan of sealing components and other critical elements.

This reaction cell, capable of XRD, XAFS, and OMS, provides a powerful and comprehensive method for studying the thermal behavior of high-nickel cathode materials.

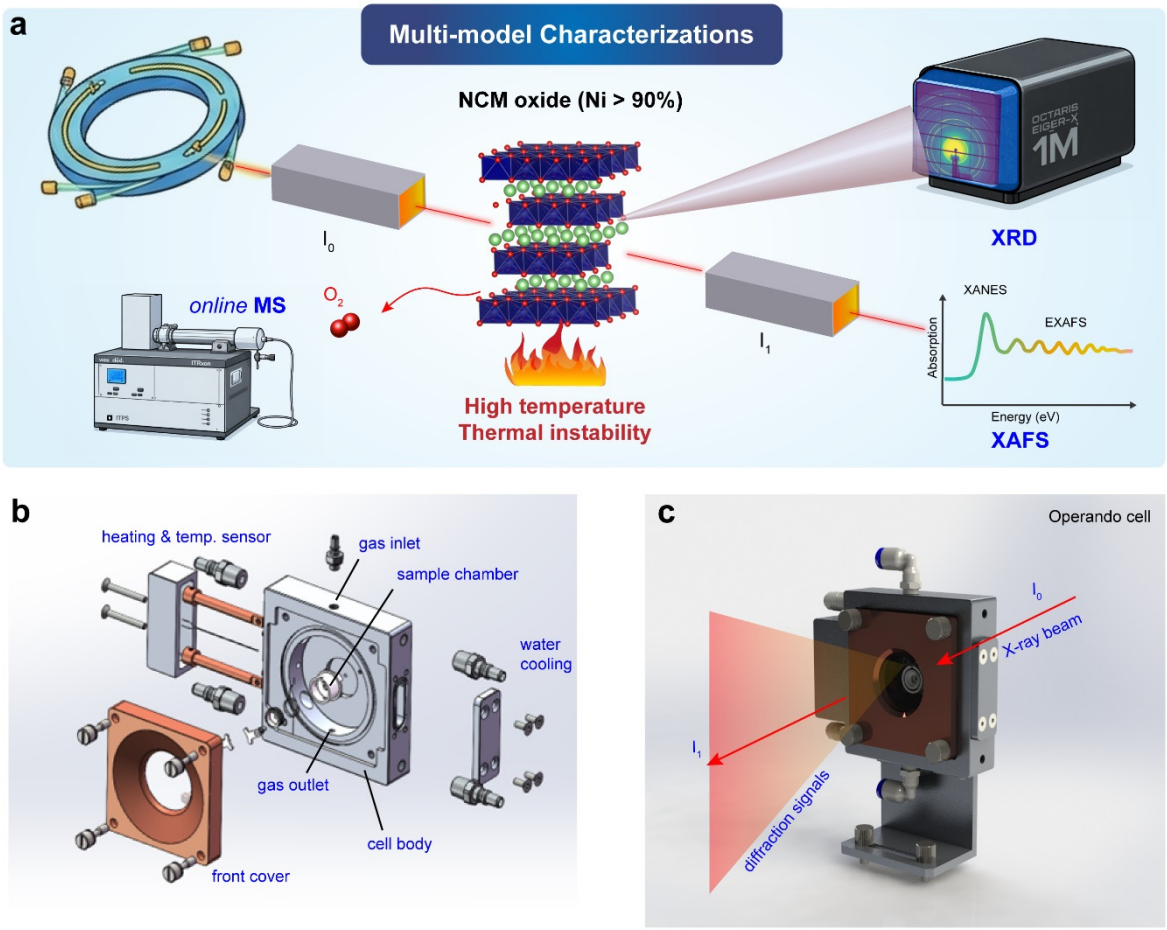

Figure 1. Schematic illustration of the multi-modal characterizations for investigating the thermal instability of high Ni cathodes. (**a**) Conceptual diagram showing the integration of *operando* XRD, XAFS, and OMS to correlate structural transitions and oxygen evolution during heating. (**b**) Exploded view of the *operando* reaction cell, highlighting the heating module, temperature sensor, gas flow channels, chamber body, and water-cooling components. (**c**) Assembled view of the *operando* cell mounted for synchrotron measurements, showing the X-ray beam path and diffraction signal collection geometry.

3. Results and Discussion

3.1. Materials Characterization

In this study, we used commercial NCM96 polycrystalline oxide as the model cathode material to demonstrate the capabilities of the system. First, we evaluated the material's structure and electrochemical performance. The NCM96 electrodes were delithiated in Li-ion cells by charging to 4.3 V at 0.1 C. The electrodes were then recovered in an Ar-filled glovebox, rinsed with anhydrous DMC, and vacuum-dried prior to thermal measurements. The charge capacity exceeded 240 mAh g^{-1}, corresponding to an estimated delithiation of ~87%. As shown in Figure 2a, the XRD pattern is well-indexed to the layered α-$NaFeO_2$-type structure with the R-3m space group [32], confirming the formation of a well-crystallized layered phase. SEM images (Figures 2b and S1) reveal that the particles exhibit a uniform single-crystal morphology with sizes in the range of 2–3 μm. As presented in Figure 2c,d, the electrode demonstrated a high initial discharge capacity reaching 240 mAh g^{-1} and stable cycling behavior over 30 cycles, retaining 88% of its capacity. Extended cycling further confirmed the electrochemical stability of the material, with ~65% capacity retention after 100 cycles at 0.1 C (Figure S3). Notably, the electrode exhibited high Coulombic efficiency throughout the cycling process. The corresponding dQ/dV curves show typical redox peaks, reflecting the characteristic voltage evolution of Ni-rich layered oxides and indicating the structural transitions occurring during Li^+ extraction and insertion.

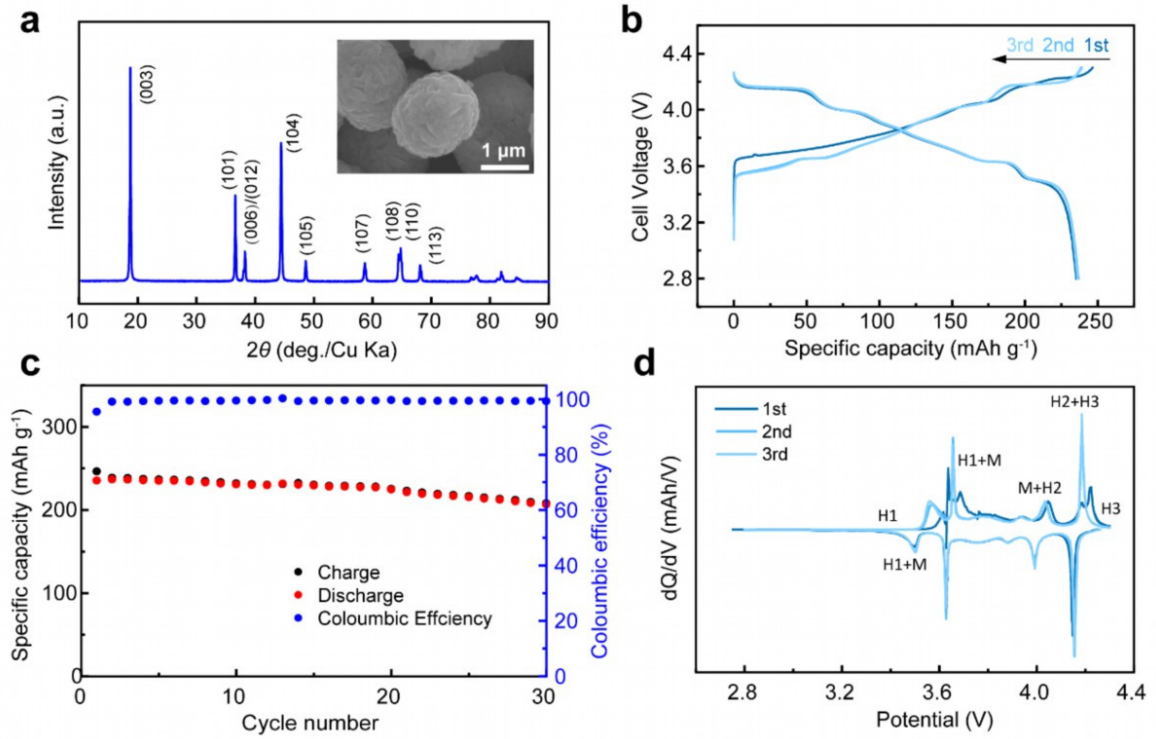

Figure 2. Structural and electrochemical characterization of the commercial NCM96 polycrystalline cathode material. (**a**) XRD pattern of the pristine material. (**b**) SEM image of the pristine NCM96 particles. (**c**) Initial charge–discharge voltage profiles at 0.1 C. (**d**) Cycling performance and coulombic efficiency of the NCM96 electrode.

3.2. Operando XRD Measurements

Operando high-temperature XRD was employed to characterize the phase transitions of delithiated NCM96 during thermal decomposition. The experimental configuration, supported by a synchrotron-based 2D detector, is shown in Figure 3a. This setup enabled high-temporal-resolution data acquisition, capturing the continuous structural evolution throughout the heating process. Representative 2D diffraction patterns (Figure 3b) illustrate the progressive phase transformations from the layered (L) phase to spinel (S) and eventually rock-salt (RS) phases. Notably, the characteristic (003) reflection of the layered structure weakens and shifts at 250 °C, signaling the formation of spinel phase. By 550 °C, this peak disappears entirely, indicating a complete transition to the rock-salt phase.

The thermal evolution of key diffraction peaks and the full-range XRD patterns (10–90°) are presented in Figures 3c and S4, respectively. The plots reveal more detailed information of structural reconstruction during heating at 5 °C min^{-1}. Below 185 °C, the material primarily retains its layered structure with minimal changes in peak position or intensity. Within the 185–220 °C range, the (003) peak exhibits a pronounced shift and rapid intensity decay, marking an acceleration in structural degradation. Above 225 °C, the emergence of spinel-related reflections indicates a critical phase-transition stage. Subsequent heating leads to the attenuation of spinel peaks after 330 °C, culminating in a disordered rock-salt phase at higher temperatures.

To better understand the triggers of irreversible thermal runaway, we focused on the early-stage structural response during heating by performing a detailed analysis of the (003) diffraction peak evolution. As shown in Figure 3f, the (003) reflection of NCM96 charged to 4.3V splits into two peaks at $2\theta \approx 18.5°$ and 19.5°, corresponding to the H2 and H3 hexagonal phases, respectively. High-nickel cathodes typically undergo a sequence of phase transitions across H1 (initial hexagonal), M (monoclinic), H2, and H3 phases [33]. In this context, the H2 phase represents moderately delithiated regions with relatively larger interplanar *d* spacing, whereas the H3 phase denotes highly delithiated domains characterized by significant lattice contraction [34]. This peak splitting confirms a pronounced structural heterogeneity within the highly delithiated NCM96 cathode.

The evolution of intensity and position for these split (003) peaks is quantified in Figure 3d,e. Between 25 °C and 180 °C, thermal expansion induces a slight shift of both peaks toward lower angles ($\Delta 2\theta \approx 0.05$–0.1°). However, the H2 and H3 components exhibit divergent thermal responses thereafter. The $(003)_{H2}$ intensity shows a transient increase before shifting toward higher angles above 180 °C and rapidly decaying beyond 200 °C. In

contrast, the $(003)_{H3}$ intensity decreases monotonically from the start of heating, while its position remains relatively stable until 220 °C. Both components eventually merge into a single spinel reflection at $2\theta \approx 18.7°$.

The transient enhancement of the H2 peak suggests a structural relaxation mechanism involving the migration of Ni^{2+} ions from the Li layer back to the transition metal (TM) layer. Simultaneously, the attenuation of the H3 peak indicates that portions of the H3 phase may revert toward an H2-like state, driven by lithium-ion diffusion from Li-rich domains into the more compressed, Li-poor H3 regions. This thermally induced cation migration significantly impacts the lattice stability, resulting in a drastic decrease in H3 peak intensity and pronounced peak broadening. These features also suggest an amorphization process within the framework, characterized by the formation of nanosized domains prior to the onset of the comprehensive transition to the spinel phase. Accordingly, the H3 region, defined by severe lithium depletion upon charging, is inherently more susceptible to the loss of long-range periodicity and localized structural instability. This vulnerability leads to the immediate intensity decay observed at the onset of heating, marking the H3 domains as the primary sites for early-stage structural degradation.

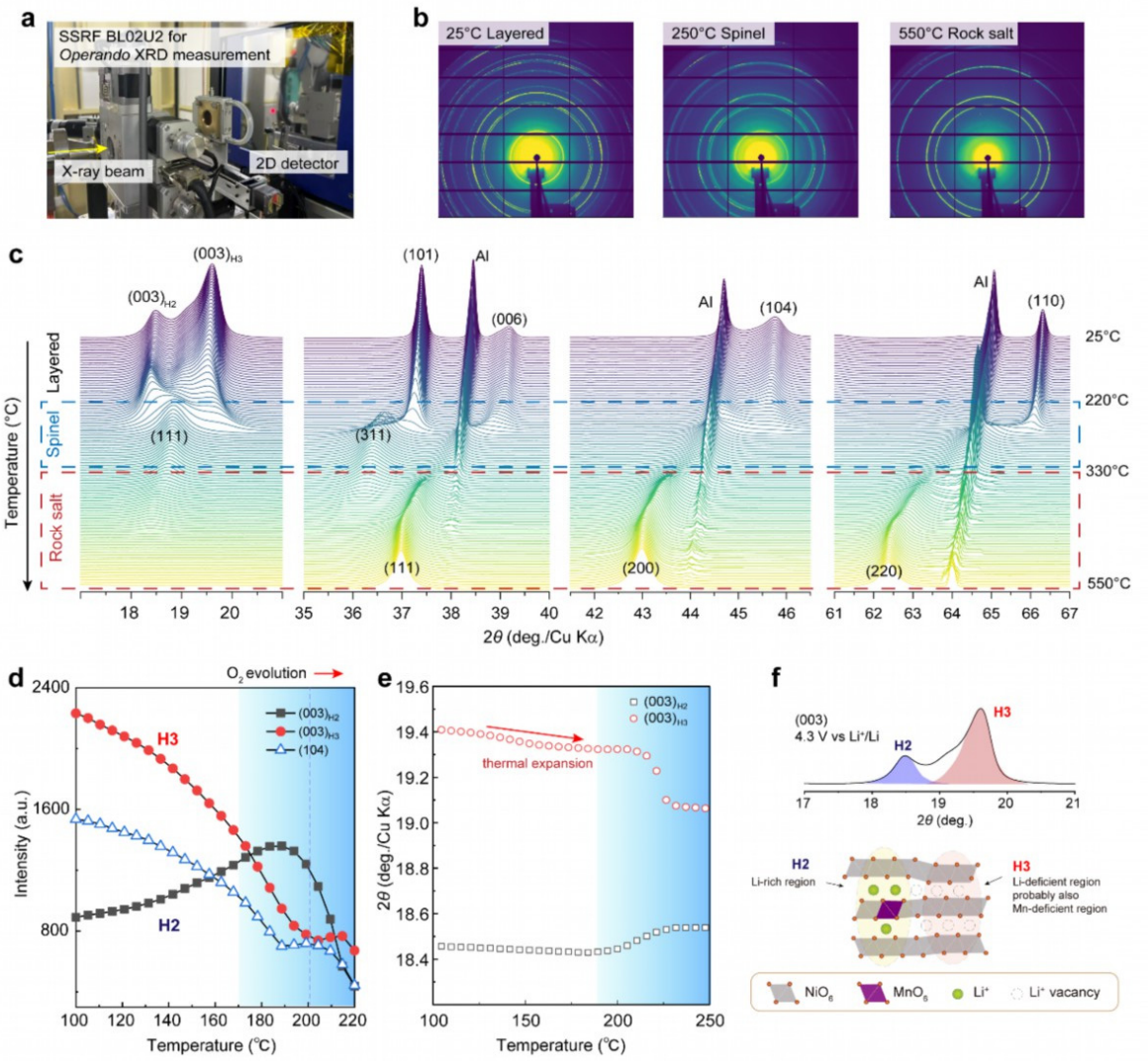

Figure 3. *Operando* synchrotron XRD analysis of delithiated NCM96 during thermal decomposition. (**a**) Photograph of the *operando* high-temperature XRD setup. (**b**) Representative 2D diffraction patterns at selected temperatures. (**c**) Temperature-dependent evolution of characteristic diffraction peaks during heating from 25 to 550 °C at 5 °C min^{-1}. (**d**) Evolution of the intensities of the split $(003)_{H2}$, $(003)_{H3}$, and (104) reflections. (**e**) Evolution of the 2θ positions of the split (003)H2 and (003)H3 reflections. (**f**) Schematic illustration of the split (003) peak and the H2- and H3-related domains in delithiated NCM96.

3.3. Operando XAFS Measurement

Figure 4 illustrates the principle of *operando* high-temperature XAFS spectroscopy and its application in tracking the thermal decomposition of delithiated NCM96. The experiments were performed at the ODE beamline (Synchrotron SOLEIL, Saint-Aubin, France) using the energy-dispersive XAFS (ED-XAFS) mode in transmission

geometry. This configuration allows for high-temporal-resolution data acquisition, critical for capturing transient intermediate states. As shown in Figure 4a, the sample was heated from room temperature to 550 °C at a ramp rate of 5 °C min^{-1} under an anhydrous Ar atmosphere to isolate the intrinsic redox behavior from environmental oxygen interference. Each spectrum was collected with an integration time of 600 ms and averaged over 200 scans to ensure a high signal-to-noise ratio (Figure 4b). To assess whether this averaging procedure obscured rapid spectral changes within the critical temperature range, the data collected between 175 and 250 °C were reprocessed using a 40-scan averaging window, corresponding to a temporal resolution of ~24 s or a temperature resolution of ~2 °C per spectrum (Figure S5). The normalized Ni K-edge XANES spectra (Figure 4c) reveal a continuous shift of the absorption edge toward lower energy levels as temperature increases. This red-shift signifies the progressive reduction of Ni^{4+} and Ni^{3+} species. The first-derivative spectra (Figure 4d) and the difference XANES plots (Figure 4f) highlight that the most significant electronic reconstruction occurs between 185 °C and 330 °C. As quantified in Figure 4g, the Ni K-edge energy drops sharply from approximately 8351 eV to 8348 eV within the 175–330 °C window. Literature suggests that this rapid reduction is intrinsically linked to the release of lattice oxygen—a process driven by the instability of the Ni^{4+}–O^{2-} bond at high delithiation states—which provides the chemical potential for transition metal reduction and subsequent oxygen evolution. Beyond 400 °C, the reduction rate plateaus, reaching a final state of approximately 8347 eV, consistent with a rock-salt-like NiO coordination environment.

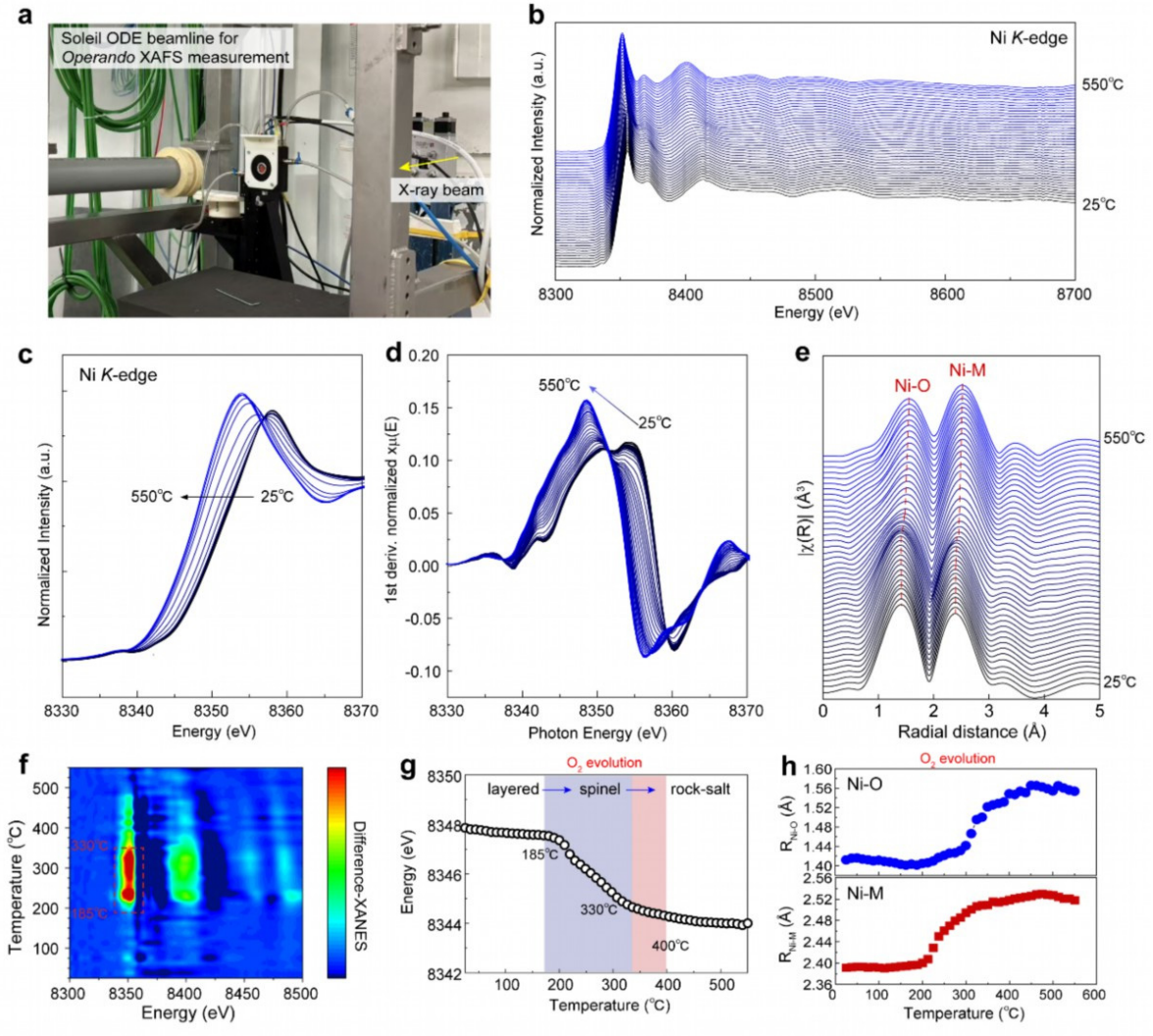

Figure 4. *Operando* Ni K-edge XAFS measurements of delithiated NCM96 during thermal decomposition. (**a**) Photograph of the *operando* high-temperature XAFS setup. (**b**) Temperature-dependent Ni K-edge XAFS spectra collected during heating. (**c**) Normalized XANES spectra and (**d**) corresponding first-derivative spectra. (**e**) Fourier-transformed EXAFS spectra in R space. (**f**) Difference XANES contour map. (**g**) Evolution of the Ni K-edge position and (**h**) Ni–O and Ni–M bonds as a function of temperature.

Beyond valence state changes, the local coordination environment undergoes profound restructuring. The Fourier-transformed (FT) EXAFS spectra in R-space (Figure 4e) exhibit a systematic evolution of the Ni–O (first

shell) and Ni–M (second shell) scattering paths. Quantitative analysis of the bond lengths (Figure 4h) indicates that both Ni–O and Ni–M distances increase significantly above 200 °C. The increase in Ni–O and Ni–M distances is consistent with the increased ionic radius associated with Ni reduction, following the trend of $R_{Ni^{4+}} < R_{Ni^{3+}} < R_{Ni^{2+}}$. Furthermore, the reduction in peak intensity in *R*-space suggests a loss of local symmetry and an increase in Debye-Waller factors, reflecting the transition from a highly ordered layered framework to a disordered spinel or rock-salt structure [35].

Although the Ni reduction process can be tracked qualitatively through the continuous shift of the absorption edge, quantitative determination of the evolving Ni valence states and identification of critical transition temperatures remain challenging. To resolve the temperature-dependent evolution of the local Ni electronic structure, the *operando* Ni K-edge XAFS dataset was analyzed using MCR-ALS (Figure S6). Three dominant spectral components were identified, corresponding to the initial charged state, an intermediate thermally transformed state, and a final reduced state. The contribution of the initial component continuously decreases with temperature, whereas the intermediate and final components emerge and grow progressively. A pronounced increase in the intermediate component occurs near 200–210 °C, closely matching the onset of the layered-to-spinel transformation revealed by *operando* XRD. This concurrence indicates that transition-metal reduction and structural reconstruction are strongly coupled processes and that substantial changes in the local Ni electronic structure accompany the early stages of thermal decomposition.

3.4. Gas Evolution and Heat Generation

To further elucidate the correlation between gas evolution and the exothermic behavior of delithiated NCM96 during thermal decomposition, OMS and DSC were performed (Figure 5). The results reveal a clear staging of thermal failure, where outgassing profiles are intrinsically linked to the material's thermodynamic instability.

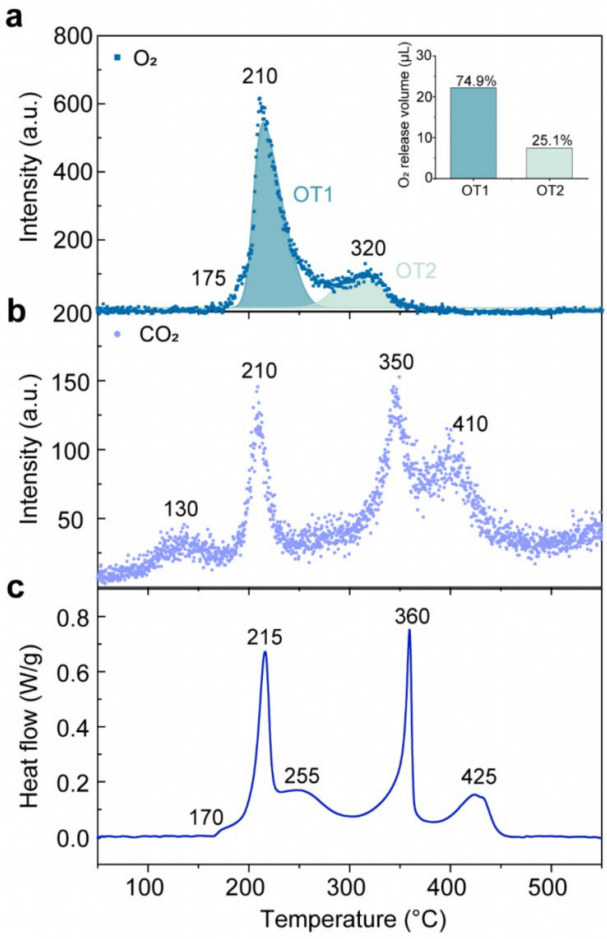

Figure 5. Correlation between gas evolution and heat release during thermal decomposition of delithiated NCM96. (**a**) O_2 evolution profile highlighting two distinct outgassing stages (O_{T1} and O_{T2}): the inset provides a quantitative comparison of their relative contributions to total oxygen release. (**b**) Temperature-resolved CO_2 evolution profile. (**c**) DSC thermogram showing the multi-stage exothermic response.

The O_2 evolution profile is primarily divided into two stages: an initial significant release beginning at ~175 °C, reaching a dominant peak at 210 °C, followed by a secondary, lower-intensity peak at 320 °C. Quantitative analysis reveals that the first stage (O_{T1}) accounts for 74.9% (22.19 μL) of the total oxygen evolved, while the second stage (O_{T2}) contributes only 25.1% (7.14 μL). This indicates that early-stage lattice oxygen loss dominates the overall gas evolution process. For comparison, the O_2 evolution behavior of NCM811 at the same charged state (4.3 V), taken from our previous work, shows a much less concentrated first-stage release, with O_{T1} accounting for only 43.2% of the total O_2 evolution, whereas the later-stage release (O_{T2}) becomes dominant (56.8%) (Figure S7) [36]. In contrast, the much larger O_{T1} contribution in NCM96 suggests that ultra-high Ni cathodes undergo a more abrupt early-stage oxygen-release process. In contrast, CO_2 release follows a more complex multi-peak pattern, with signals at 130, 210, 350, and 410 °C. The broad peak at 130 °C is likely ascribed to the decomposition of surface carbonate species and SEI components [37]. Meanwhile, the signals at 350 °C and 410 °C are attributed to the thermal degradation of the PVDF binder [38].

The DSC thermogram corroborates these findings, identifying primary exothermic peaks at 215 °C and 360 °C, with minor heat release events near 255 °C and 425 °C. The precise thermal alignment between the first O_2 release peak (O_{T1}) and the primary exothermic peak confirms that initial lattice oxygen evolution is the fundamental trigger for the vigorous heat generation.

It is worth noting that the thermal measurements were performed on charged composite NCM96 electrodes consisting of NCM96 active material, carbon black, and PVDF binder in a mass ratio of 8:1:1. Consequently, the evolution of carbon-containing gases, particularly CO_2, may partially originate from the thermal decomposition or oxidation of conductive carbon and PVDF in addition to reactions involving the NCM oxide itself. While oxygen release is substantially suppressed during the second decomposition stage, the continued evolution of CO_2 accompanied by a secondary exothermic peak suggests that thermal reactions remain active at elevated temperatures.

3.5. Thermal Decomposition Mechanisms of Ultra-High Ni NCM Cathodes

The most catastrophic degradation occurs between 210 °C and 255 °C, where the *operando* XRD (layered-to-spinel transition), XAFS (accelerated Ni reduction), OMS (rapid O_2 evolution), and DSC (primary exotherm) profiles converge. This synchronized behavior suggests a "thermal snap" effect. Here, thermal snap refers to a narrow temperature interval in which Ni reduction, lattice oxygen release, and long-range structural collapse occur in a highly synchronized manner, marking the abrupt transition from gradual thermal degradation to rapid framework failure.

Prior to this transition, *operando* XRD reveals a transient enhancement of the H2 phase accompanied by a continuous intensity decay of the H3 phase at the early heating stage, indicating that local structural perturbations and cation rearrangements occur before bulk phase transition. Interestingly, *operando* XANES also shows that Ni reduction begins at ~175 °C, coinciding with the onset of O_2 evolution. The temporal separation between the initiation of Ni reduction and the subsequent layered-to-spinel phase transition suggests the existence of an intermediate stage characterized by local electronic and structural instability.

In highly delithiated ultra-high-Ni NCM cathodes, Ni^{4+} exist in a metastable oxidation state that is particularly sensitive to thermal perturbation. The initial reduction of Ni^{4+} to Ni^{3+}/Ni^{2+} may weaken the metal–oxygen framework and promote oxygen-vacancy formation. The resulting Ni^{2+} species are prone to migrate into Li layers and induce local cation disorder without immediately triggering a detectable crystallographic phase transition. These observations suggest that thermal decomposition is initiated by local electronic instability and oxygen-sublattice destabilization, which subsequently evolve into extensive cation migration, oxygen release, and large-scale structural reconstruction. Further DFT calculations and advanced spectroscopies are needed to elucidate the formation mechanisms and local properties of oxygen vacancies and transient oxygen species during this critical intermediate stage, and to determine their role in initiating thermal runaway.

4. Conclusions

In summary, we have systematically investigated the thermal decomposition mechanisms of delithiated NCM96 using a suite of *operando* characterization techniques. The integration of long-range crystalline information (XRD), local electronic and coordination environments (XAFS), and real-time outgassing behaviors (OMS) allows for a multi-scale understanding of the failure pathway.

We demonstrate that thermal runaway is not a sequence of isolated events, but a tightly coupled "chemical-mechanical-thermal" feedback loop. The H3 domains, characterized by severe lithium depletion, serve as the "weak links" where amorphization and local instability first emerge, eventually nucleating the transition to the spinel phase. The catastrophic failure at approximately 210 °C is a critical point where oxygen evolution, Ni

reduction, and layered-to-spinel transitions occur in a self-accelerating, exothermic feedback loop. The fact that nearly 75% of oxygen release occurs in this narrow window underscores the violent nature of the initial structural collapse.

These insights emphasize that enhancing the thermal stability of high-nickel cathodes requires not only global structural stabilization but also the mitigation of local electronic instability and the suppression of transition metal migration. This work highlights the power of multimodal *operando* techniques in deconstructing complex battery failure mechanisms, providing critical guidance for the engineering of safer high-capacity electrode materials.

Supplementary Materials

The additional data and information can be downloaded at: https://media.sciltp.com/articles/others/260609 1606486397/AC-26040184-SM-final.pdf. Figure S1. SEM images of pristine NCM96 powder: (a,b) images at different magnifications. Figure S2. SEM images of delithiated NCM96 (charged to 4.3 V) at different temperatures: (a) room temperature; (b) 175 °C; and (c) 220 °C. Figure S3. Long-term cycling performance of NCM96 measured at 0.1 C between 2.8 and 4.3 V for 100 cycles. Figure S4. Full-pattern *operando* XRD evolution of delithiated NCM96 (Cu Kα equivalent, 10–90°) during heating from 25 to 550 °C at 5 °C min^{-1}. The dashed lines mark selected characteristic temperatures during thermal decomposition. Figure S5. Reprocessed Ni K-edge evolution of delithiated NCM96 during heating. (a) Temperature-dependent Ni K-edge position extracted from the operando ED-XAFS spectra processed using 200-frame averaging. The red box highlights the critical temperature region from 175 to 250 °C. (b) Enlarged Ni K-edge position evolution in the 175–250 °C region reprocessed using 40-frame averaging. Figure S6. Temperature-dependent evolution of Ni K-edge XAFS components in delithiated NCM96 resolved by MCR-ALS: Component 1—initial charged state; Component 2—intermediate thermally evolved state; Component 3—final high-temperature state. Figure S7. Comparison of O_2 evolution behavior between delithiated NCM96 and NCM811 at 4.3 V. (a) OMS profile and quantitative contribution of the two oxygen-release stages for NCM96; (b) Corresponding OMS result for NCM811 at 4.3 V, adapted from our previous work.

Author Contributions

Y.Z.: investigation, data curation, writing—original draft preparation; H.L.: investigation, draft preparation; Z.L: conceptualization, methodology; C.W.: formal analysis; W.S.: investigation; W.Z.: data curation; J.H.: methodology, writing—reviewing and editing; C.Y.: project administration, funding acquisition, writing—reviewing and editing. All authors have read and agreed to the published version of the manuscript.

Funding

This research was funded by Fujian science & technology innovation laboratory for energy devices of China (21C LAB). (The data of X-ray absorption spectroscopy were obtained on beamline ODE under proposal 20250601 and 20250973).

Institutional Review Board Statement

Not applicable.

Informed Consent Statement

Not applicable.

Data Availability Statement

Additional experimental photos, SEM images, battery performance and *operando* XRD evolution profiles are provided in the supporting information.

Acknowledgments

We thank the Shanghai Synchrotron Radiation Facility of BL02U2 (https://cstr.cn/31124.02.SSRF.BL02U2) for the assistance on XRD measurements. We acknowledge SOLEIL for provision of synchrotron radiation facilities and we would like to thank the assistance from SOLEIL beamline staff.

Conflicts of Interest

The authors declare no competing interests.

Use of AI and AI-Assisted Technologies

No AI tools were utilized for this paper.

References

1. Meng, D.; Shi, X.; Jiang, J.; et al. Experimental Study on Thermal Runaway Propagation Characteristics and Combustion Behaviors of LFP and NCM Lithium-Ion Batteries Induced by Dual Heat Sources. *Appl. Therm. Eng.* **2026**, *294*, 130589. https://doi.org/10.1016/j.applthermaleng.2026.130589.
2. Ren, X.; Kong, D.; Ping, P.; et al. Experimental Study on the Evolution Patterns of Thermal Runaway and Safety Boundaries of Commercial Lithium-Ion Batteries under Overheating Failure. *Mater. Today Energy* **2025**, *52*, 101937. https://doi.org/10.1016/j.mtener.2025.101937.
3. Ma, L.; He, Y.; Zhang, J.; et al. Experimental Study on Thermal Runaway Characteristics and Propagation Mechanisms of Large-Capacity NCM Batteries Triggered by Overheating under Charging Conditions. *Process Saf. Environ. Prot.* **2025**, *202*, 107719. https://doi.org/10.1016/j.psep.2025.107719.
4. Maleki, H.; Howard, J.N. Internal Short Circuit in Li-Ion Cells. *J. Power Sources* **2009**, *191*, 568–574. https://doi.org/10.1016/j.jpowsour.2009.02.070.
5. Wang, H.; Lara-Curzio, E.; Rule, E.T.; et al. Mechanical Abuse Simulation and Thermal Runaway Risks of Large-Format Li-Ion Batteries. *J. Power Sources* **2017**, *342*, 913–920. https://doi.org/10.1016/j.jpowsour.2016.12.111.
6. Zhao, H.; Bo, X.K.; Zhang, Z.G.; et al. Insight into Puncture-Induced Thermal Runaway in Lithium-Ion Batteries to Reduce Fire Risks in Electric Vehicle Collisions. *Battery Energy* **2025**, *4*, e70041. https://doi.org/10.1002/bte2.20250036.
7. Jia, Y.; Yue, Y.; Xu, W.; et al. Thermal Runaway Features of Prismatic NCM Battery Undergone High-Rate Charging/Discharging: Mechanism Investigation and Safety Evaluation. *Appl. Therm. Eng.* **2025**, *275*, 126634. https://doi.org/10.1016/j.applthermaleng.2025.126634.
8. Chen, J.; Xu, C.; Wang, Q.; et al. The Thermal-Gas Coupling Mechanism of Lithium Iron Phosphate Batteries during Thermal Runaway. *J. Power Sources* **2025**, *625*, 235728. https://doi.org/10.1016/j.jpowsour.2024.235728.
9. Ouyang, D.X.; Chen, M.Y.; Weng, J.W.; et al. Exploring the Thermal Stability of Lithium-Ion Cells via Accelerating Rate Calorimetry: A Review. *J. Energy Chem.* **2023**, *81*, 543–573. https://doi.org/10.1016/j.jechem.2023.02.030.
10. Jiang, Z.-J.; Luo, Z.-H.; Guo, J.-X.; et al. Thermal Safety Overview of Silicon-Carbon Anode in Lithium-Ion Batteries: Key Parameters in Determining the Reactivity. *Particuology* **2025**, *100*, 178–185. https://doi.org/10.1016/j.partic.2025.03.013.
11. Zhu, X.Q.; Wang, H.; Wang, X.; et al. Internal Short Circuit and Failure Mechanisms of Lithium-Ion Pouch Cells under Mechanical Indentation Abuse Conditions: An Experimental Study. *J. Power Sources* **2020**, *455*, 227939. https://doi.org/10.1016/j.jpowsour.2020.227939.
12. Barkholtz, H.M.; Preger, Y.; Ivanov, S.; et al. Multi-Scale Thermal Stability Study of Commercial Lithium-Ion Batteries as a Function of Cathode Chemistry and State-of-Charge. *J. Power Sources* **2019**, *435*, 226777. https://doi.org/10.1016/j.jpowsour.2019.226777.
13. Jo, S.; Seo, S.; Kang, S.K.; et al. Thermal Runaway Mechanism in Ni-Rich Cathode Full Cells of Lithium-Ion Batteries: The Role of Multidirectional Crosstalk. *Adv. Mater.* **2024**, *36*, e2402024. https://doi.org/10.1002/adma.202402024.
14. Zhou, W.; Zhang, Y.; Wang, C.; et al. Rare-Earth Oxide Additives Mitigate Oxygen Release and Thermal Runaway in Ni-Rich NCM Cathodes. *J. Rare Earths* **2026**, in press. https://doi.org/10.1016/j.jre.2026.03.010.
15. Bak, S.M.; Hu, E.Y.; Zhou, Y.N.; et al. Structural Changes and Thermal Stability of Charged $LiNi_xMn_yCo_ZO_2$ Cathode Materials Studied by Combined *In Situ* Time-Resolved XRD and Mass Spectroscopy. *ACS Appl. Mater. Interfaces* **2014**, *6*, 22594–22601. https://doi.org/10.1021/am506712c.
16. Mai, A.N.T.; Chern, C.-S.; Kuss, C.; et al. Enhancing Thermal Properties and Electrochemical Performance of $LiNi_{0.6}Co_{0.2}Mn_{0.2}O_2$ Cathode with Bismaleimide-Cyanuric Acid Polymer Coating for Safer Lithium-Ion Batteries. *Mater. Today Commun.* **2025**, *47*, 113033. https://doi.org/10.1016/j.mtcomm.2025.113033.
17. Cui, Z.H.; Manthiram, A. Thermal Stability and Outgassing Behaviors of High-Nickel Cathodes in Lithium-Ion Batteries. *Angew. Chem. Int. Ed.* **2023**, *62*, e202307243. https://doi.org/10.1002/anie.202307243.
18. Liu, X.; Xu, G.L.; Yin, L.; et al. Probing the Thermal-Driven Structural and Chemical Degradation of Ni-Rich Layered Cathodes by Co/Mn Exchange. *J. Am. Chem. Soc.* **2020**, *142*, 19745–19753. https://doi.org/10.1021/jacs.0c09961.
19. Peiris, M.D.H.C.; Liepinya, D.; Liu, H.; et al. Electrolyte Reactivity, Oxygen States, and Degradation Mechanisms of Nickel-Rich Cathodes. *Cell Rep. Phys. Sci.* **2024**, *5*, 102039. https://doi.org/10.1016/j.xcrp.2024.102039.
20. Zhang, B.; Zhang, H.Y.; Su, Y.F.; et al. Rare-Earth Doping Induced Pinning Effect with Enhanced Chemo-Mechanical Stability in Ni-Rich Cathodes for Lithium-Ion Batteries. *Chin. J. Chem.* **2025**, *43*, 889–896. https://doi.org/10.1002/cjoc.202401071.
21. Liu, J.Z.; Dong, J.Y.; Wang, M.; et al. Redox-Active Stabilizer-Enhanced Structural and Thermal Stability of Ni-Rich Cathodes via an Economical Blending Strategy. *eTransportation* **2025**, *24*, 100428. https://doi.org/10.1016/j.etran.2025.100428.

22. Liang, Y.Z.; Xue, H.Y.; Zhan, M.Z.; et al. Stationary Oxygen Vacancy Construction toward a Superior-Performance Ultrahigh Nickel Single-Crystal Cathode. *ACS Nano* **2025**, *19*, 25879–25889. https://doi.org/10.1021/acsnano.5c05412.
23. Jiang, Z.X.; Liu, C.G.; Huang, L.; et al. Interfacial Reactions Take the Lead: Elucidating the Dominant Role of Cathode-Electrolyte Interactions in Triggering Thermal Runaway of High-Nickel Lithium-Ion Batteries. *Energy Environ. Sci.* **2025**, *18*, 8232–8243. https://doi.org/10.1039/d5ee01431j.
24. Song, Y.J.; Cui, Y.P.; Li, B.Y.; et al. Revealing the Origin of High-Thermal-Stability of Single-Crystal Ni-Rich Cathodes toward Higher-Safety Batteries. *Nano Energy* **2023**, *116*, 108846. https://doi.org/10.1016/j.nanoen.2023.108846.
25. Wang, C.; Zhang, R.; Kisslinger, K.; et al. Atomic-Scale Observation of O1 Faulted Phase-Induced Deactivation of $LiNiO_2$ at High Voltage. *Nano Lett.* **2021**, *21*, 3657–3663. https://doi.org/10.1021/acs.nanolett.1c00862.
26. Hu, E.; Bak, S.-M.; Liu, J.; et al. Oxygen-Release-Related Thermal Stability and Decomposition Pathways of $Li_xNi_{0.5}Mn_{1.5}O_4$ Cathode Materials. *Chem. Mater.* **2013**, *26*, 1108–1118. https://doi.org/10.1021/cm403400y.
27. Britala, L.; Marinaro, M.; Kucinskis, G. A Review of the Degradation Mechanisms of NCM Cathodes and Corresponding Mitigation Strategies. *J. Energy Storage* **2023**, *73*, 108875. https://doi.org/10.1016/j.est.2023.108875.
28. Wang, Y.; Ren, D.; Feng, X.; et al. Thermal Kinetics Comparison of Delithiated $Li[Ni_xCo_yMn_{1-x-y}]O_2$ Cathodes. *J. Power Sources* **2021**, *514*, 230582. https://doi.org/10.1016/j.jpowsour.2021.230582.
29. Wei, Z.S.; Liang, C.; Jiang, L.H.; et al. Probing the Thermal Degradation Mechanism of Polycrystalline and Single-Crystal $Li(Ni_{0.8}Co_{0.1}Mn_{0.1})O_2$ Cathodes from the Perspective of Oxygen Vacancy Diffusion. *Energy Storage Mater.* **2023**, *56*, 495–505. https://doi.org/10.1016/j.ensm.2023.01.029.
30. da Silva, S.P.; Sita, L.E.; dos Santos, C.S.; et al. Effects on the Phases and Crystalline Structures of $LiCoO_2$ Cathode under Thermal Treatments up to 400 °C. *J. Alloys Compd.* **2019**, *810*, 151933. https://doi.org/10.1016/j.jallcom.2019.151933.
31. Wang, C.Y.; Wang, X.L.; Zhang, R.; et al. Resolving Complex Intralayer Transition Motifs in High-Ni-Content Layered Cathode Materials for Lithium-Ion Batteries. *Nat. Mater.* **2023**, *22*, 235–241. https://doi.org/10.1038/s41563-022-01461-5.
32. Park, G.T.; Ryu, H.H.; Park, N.Y.; et al. Single-Crystal vs. Polycrystalline Cathodes for Lithium-Ion Batteries. *Chem. Rev.* **2025**, *125*, 9930–10000. https://doi.org/10.1021/acs.chemrev.5c00441.
33. Wang, C.; Zhang, Y.; Li, Z.; et al. A Comprehensive Understanding of the Structural Evolution and Capacity Contribution of Fast-Charging NCM Cathodes. *J. Energy Chem.* **2026**, *114*, 183–193. https://doi.org/10.1016/j.jechem.2025.09.066.
34. Li, Y.; Gao, D.; Chang, C.; et al. Improved Electrochemical Performance of Nb^{5+} Doped NCM Cathode upon 4.5 V Application Beneficial from the Suppressed H2-H3 Phase Transition and Promoted Li^+ Migration Kinetics. *J. Energy Storage* **2023**, *73*, 109139. https://doi.org/10.1016/j.est.2023.109139.
35. Zhang, F.; Lou, S.; Li, S.; et al. Surface Regulation Enables High Stability of Single-Crystal Lithium-Ion Cathodes at High Voltage. *Nat. Commun.* **2020**, *11*, 3050. https://doi.org/10.1038/s41467-020-16824-2.
36. Zhang, Y.; Wang, C.; Zhang, J.; et al. Structural Evolution and Thermal Behavior of High-Ni Cathodes: Coupled Operando XAS, XRD, and Mass Spectrometry Analysis. *ACS Energy Lett.* **2026**, *11*, 3936–3944. https://doi.org/10.1021/acsenergylett.6c00367.
37. Zhao, J.; Ma, L.; Zhao, L.; et al. Experimental Study on Thermal Runaway Characteristics and Gas Generation Behavior Induced by Overcharge: Single Cells and Modules of Large-Capacity NCM Lithium-Ion Battery. *J. Energy Storage* **2025**, *133*, 117925. https://doi.org/10.1016/j.est.2025.117925.
38. Chen, K.; Zhang, D.; Guo, J.-X.; et al. Hydrogen Generated from Binders: An Overlooked Thermal Runaway Source in Lithium-Ion Batteries. *J. Energy Chem.* **2025**, *109*, 602–608. https://doi.org/10.1016/j.jechem.2025.06.004.